N- and *P*-type symmetric scaling behavior of monolayer hydrogenated boron arsenide transistors

Qiuhui Li,[1,*] Tao Zheng,[1,*] Lin Xu,[2,*] Shibo Fang,[1] Zongmeng Yang,[1] Linqiang Xu,[1] Ying Li,[1] Baochun Wu,[1] Xingyue Yang,[1] Ruge Quhe,[3] Guo Ying,[4] and Jing Lu[1,5,6,7,8,9,†]

[1]*State Key Laboratory for Mesoscopic Physics and Department of Physics, Peking University, Beijing 100871, People's Republic of China*
[2]*Department of Chemistry, The University of Hong Kong, Hong Kong 999077, People's Republic of China*
[3]*State Key Laboratory of Information Photonics and Optical Communications and School of Science, Beijing University of Posts and Telecommunications, Beijing 100876, People's Republic of China*
[4]*School of Physics and Telecommunication Engineering, Shaanxi Key Laboratory of Catalysis, Shaanxi University of Technology, Hanzhong 723001, People's Republic of China*
[5]*School of Integrated Circuits, Peking University, Beijing 100871, People's Republic of China*
[6]*Collaborative Innovation Center of Quantum Matter, Beijing 100871, People's Republic of China*
[7]*Beijing Key Laboratory for Magnetoelectric Materials and Devices, Beijing 100871, People's Republic of China*
[8]*Peking University Yangtze Delta Institute of Optoelectronics, Nantong 226000, People's Republic of China*
[9]*Key Laboratory for the Physics and Chemistry of Nanodevices, Peking University, Beijing 100871, People's Republic of China*

(Received 29 September 2023; accepted 8 January 2024; published 26 January 2024)

High thermal conductivity and ambipolar mobility are highly desirable for semiconductors in electronics and have been observed in bulk boron arsenide (BAs). In this work, we explore the scaling behavior of a monolayer hydrogenated BAs field-effect transistor (ML H-BAs FET) by employing *ab initio* quantum transport methods. Both the armchair- and zigzag-directed ML H-BAs FETs can well satisfy the requirements of the International Technology Roadmap for Semiconductors even if the gate length is scaled down to 2 ∼ 3 nm for high-performance applications. The excellent *n*- and *p*-type symmetry of bulk BAs is well preserved in the ML H-BAs FET along with the zigzag direction but is lost in the armchair direction. However, such asymmetry can be suppressed by applying uniaxial compressive strain owing to the broken valence band degeneracy. Our findings provide important theoretical insights into transport symmetry and the scaling behavior of ML H-BAs FETs.

DOI: 10.1103/PhysRevMaterials.8.014603

I. INTRODUCTION

Complementary metal-oxide-semiconductor (CMOS) is a key component of integrated circuits (ICs) owing to low static power consumption, high noise immunity, and a large output voltage swing [1,2]. Both high electron mobility (μ_e) and hole mobility (μ_h) are desired for semiconductor channel materials to ensure effective logical operation of CMOS ICs [3]. Downscaling the transistors and improving the integration level is the driving force to promote the development of CMOS ICs [4]. However, the corresponding heat generated per unit volume in CMOS ICs rapidly increases, degrading device operation and energy efficiency [5,6]. Using semiconductor channel materials with high thermal conductivity can effectively dissipate heat and extend the lifetime of transistors [6,7]. Therefore, it is highly desirable to search for a kind of semiconductor with simultaneously high ambipolar mobility and high thermal conductivity.

Nowadays, bulk boron arsenide (BAs) have been verified as the only known semiconductor with this combination of those properties [3,8]. Bulk BAs exhibits an extremely high ambipolar mobility of $1600\,\mathrm{cm^2\,V^{-1}\,s^{-1}}$ and ultrahigh thermal conductivity of $1200\,\mathrm{W\,m^{-1}\,K^{-1}}$ [3,8]. One question arises naturally: what is the scaling limit of the BAs field-effect transistors (FETs) and can the BAs FETs maintain good symmetry of $n-$ and p-type FETs with the downscaling gate length? The gate controllability can be characterized by the natural length ($\lambda \propto \sqrt{t_{ch}}$) [1,4], and λ decreases with decreasing channel thickness t_{ch}. Therefore, reducing t_{ch} has been considered an effective method to enhance gate control and extend the scaling limit [1,4,9]. As the limiting form of BAs, monolayer hydrogenated BAs (ML H-BAs) has been predicted to be dynamically stable [10,11]. Simulating the ML H-BAs FETs is expected to reach the ultimate scaling limit of BAs FETs.

In this work, we predict the transport properties of ML H-BAs FETs by employing *ab initio* quantum transport methods. Both the armchair- and zigzag-directed ML H-BAs FETs can well satisfy the requirements of the International Technology Roadmap for Semiconductors (ITRS) even if the gate length is scaled down to 2 and 3 nm, respectively. Remarkably, the excellent *n*- and *p*-type symmetry of bulk BAs is well preserved in the ML H-BAs FET along with the zigzag direction. On the other hand, the symmetry of the armchair-directed *n*- and *p*-types is not well maintained due to the asymmetric hole m_h^* and electron m_e^* effective mass ($m_h^* > m_e^*$). By

*These authors contributed equally to this work.
†Corresponding author: jinglu@pku.edu.cn

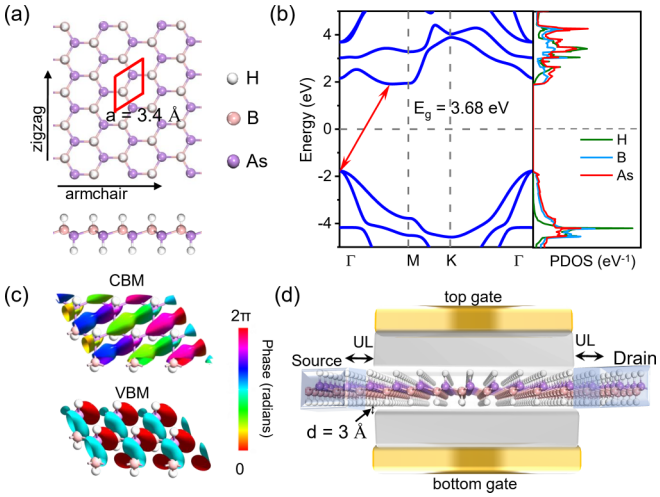

FIG. 1. (a) Top and side views of the ML H-BAs. (b) The electronic band structures and density of states (DOS) of the monolayer H-BAs. (c) The eigenstates for the conduction band minimum (CBM) and valence band maximum (VBM) of the ML H-BAs. (d) The schematic view of the DG ML H-BAs with the underlap (UL) structure.

introducing uniaxial compressive strain, such asymmetry is depressed owing to the reduced hole effective mass caused by the broken valence band degeneracy. Both the armchair- and zigzag-directed ML H-BAs FETs also show extremely low energy-delay production among the typical ML MOSFETs, making them very promising for future CMOS ICs with low energy dissipation.

II. METHOD

The passivation ensures that the dangling bonds are saturated, avoids additional defects, and finally improves the field-effect mobility for the ultrathin III-V compound semiconductor FETs [12–14]. Following comprehensive investigations involving phonon spectra, molecular dynamics simulations, and cohesive energy analysis, hydrogenated BAs has been predicted to effectively eliminate negative frequencies in the phonon spectra, enhancing structural integrity and maintaining stability under high-temperature conditions. [11] The ML BAs with H-atom passivation are optimized using the density-functional theory (DFT) method implemented in the Vienna *ab initio* simulation package (VASP), and the generalized gradient approximation (GGA) of the Perdew-Burke-Ernzerhof (PBE) exchange-correlation functional is used [15]. The optimized structure is shown in Fig. 1(a). The plane-wave cutoff energy is 400 eV, and the Monkhorst-Pack $\boldsymbol{k}$ -point mesh is $6 \times 6 \times 1$. The force tolerance on each atom and the converged energy are both less than 10^{-3} eV Å^{-1} and 10^{-6} eV, respectively. The electronic properties including band structures, the density of states (DOS), and the Bloch state of bands of ML H-BAs are calculated using the GGA-PBE level in the QuantumWise ATK package [16,17], as shown in Figs. 1(b) and 1(c). The electron and hole effective mass (m_e^* and m_h^*) is calculated by the equation $\frac{1}{m^*} = \frac{1}{\hbar}\frac{d^2E}{dk^2}$, as shown in Table I. The m_e^* and m_h^* along with the armchair(zigzag) directions are 0.17 and 0.44 (0.47 and 0.43) m_0, respectively.

TABLE I. Electron and hole effective mass of ML H-BAs along with the armchair and zigzag directions.

	Armchair	Zigzag
Electron effective mass (m_0)	0.17	0.47
Hole effective mass (m_0)	0.44	0.43

The ITRS 2013 version is used to estimate the scaling behavior of the sub-5-nm-gate-length (L_g) transistors. The reason is that it has more stringent performance metrics and shorter channel length scaling compared to the newest International Roadmap for Devices and Systems (IRDS) 2022 version [18,19]. However, the shortest L_g standard of the ITRS 2013 is 5 nm. To ensure that the standard is more precise for the sub-5-nm L_g region, we fit the figures of merit (FOMs) in the sub-5-nm L_g region for ITRS 2013. The fitted values of the FOM standards in the sub-5-nm L_g region are adopted in this work (see Fig. S1 and Table S1 in the Supplemental Material for details) [20].

The transistor model of the double-gated (DG) ML H-BAs MOSFET is shown in Fig. 1(d). The scaling behavior of the DG ML H-BAs MOSFET is calculated using DFT combined with the nonequilibrium Green's function (NEGF) formalism in the QuantumWise ATK package [16,17]. The retarded Green's function $G_{k_{//}}(E)$ is represented as:

$$G_{k_{//}}(E) = \left[(E+i\delta_+)S_{k_{//}} - H_{k_{//}} - \sum_{k_{//}}^{s}(E) - \sum_{k_{//}}^{d}(E)\right]^{-1}, \quad (1)$$

where $k_{//}$ represents the reciprocal lattice vector orthogonal to the z direction in the irreducible Brillouin zone (IBZ). s and d is the source drain electrode, respectively. $S_{k_{//}}$ and $H_{k_{//}}$ are the overlap matrix and Hamiltonian matrix, respectively. δ_+ is an infinitesimal positive number. $\sum_{k_{//}}^{s(d)}$ is the self-energy of the source(drain) electrode ($\sum_{k_{//}}^{s(d)} = \tau_{s(d)} G_{k_{//}}^{s(d)} \tau_{s(d)}^{+}$), indicating the effect of the electrodes on the carrier transport in the channel region. $\tau_{s(d)}$ is the interaction between the source(drain) electrode and the channel region. The transmission coefficient $T_{k_{//}}(E)$ is represented as

$$T_{k_{//}}(E) = Tr\left[G_{k_{//}}(E)\Gamma_{k_{//}}^{s}(E)(G_{k_{//}}(E)^{\dagger})\Gamma_{k_{//}}^{d}(E)\right]. \quad (2)$$

The broadening function $\Gamma_{k_{//}}^{s(d)} = i[\sum_{k_{//}}^{s(d)} - (\sum_{k_{//}}^{s(d)})^{\dagger}]$ represents the imaginary part of the self-energy [21]. The density matrix in the channel region is defined as $\rho_{k_{//}} = \frac{1}{2\pi}\int(f_{k_{//}}^{s} G_{k_{//}} \Gamma_{k_{//}}^{s} G_{k_{//}}^{+} + f_{k_{//}}^{d} G_{k_{//}} \Gamma_{k_{//}}^{d} G_{k_{//}}^{+})dE$, where $f_{s(d)}$ and $\mu_{s(d)}$ are the Fermi-Dirac distribution functions and electrochemical potential for the source (drain), respectively. The transport current is calculated using the Landauer formula: [22]

$$I_{ds} = \frac{2e}{h}\int_{-\infty}^{+\infty} T(E,V_b,V_g)[f_d(E-\mu_d) - f_s(E-\mu_s)]dE. \quad (3)$$

The transmission function $T(E,V_b,V_g)$ is the average of $T_{k_{//}}(E,V_b,V_g)$ over the IBZ. In terms of the fitted data of the

ITRS, the bias voltage (V_b) is fixed to 0.64 ∼ 0.55 eV when L_g is scaled from 5 to 1 nm. V_b is equal to $(\mu_s - \mu_d)/e$, and s(d) is the source(drain) of the FETs. V_g is the gate voltage. The device is simulated using a real-space density mesh cutoff of 100 Hartree, and a **k**−point mesh of 28 × 28 × 151 and 28 × 28 × 1 for the electrodes and channel, respectively. The electrodes are set to 300 K. The atomic compensation charge method is used as the doping method [23,24]. The corresponding carrier doping concentrations are tested (see Fig. S2 in the Supplemental Material for details) [20]. The optimal doping concentration can enable steep *I*-*V* curves and high-driven currents, and the corresponding optimal doping concentrations for the *n*(*p*)-type ML H-BAs MOSFETs along with the armchair and zigzag directions are 1.5(0.5) × 10^{14} cm^{-2} and 1.5(1.5) × 10^{14} cm^{-2}, respectively. The underlap (UL) structure is the undoped channel region between the gate edge and the electrode along the transport direction, as shown in Fig. 1(d). The UL technology is used to improve the immunity against the short-channel effect both in the simulations and experiments. An appropriate UL length (L_{UL}) could elevate the on-state current (I_{on}) by reducing the leakage current [23,25,26]. Moreover, the distance between the gates and the channel along the vertical direction is about 3 Å, as shown in Fig. 1(d).

The DFT-GGA method can be an accurate method to describe the exchange and correlation interaction in ultrathin FETs. The main reason is that the shielding effect is improved in the ultrathin FETs, and the band gap of the channel material is effectively renormalized to the DFT-GGA level [15,27,28]. First, such a shielding effect is caused by the dielectric layer [27]. For instance, the band gap (E_g) of ML MoS_2 at the GW level is renormalized to 1.9 eV when coupled with a high-dielectric-constant (κ_E) dielectric layer, consistent with the DFT-GGA value of 1.76 eV [29,30]. Additionally, the shielding effect is caused by carrier injection. When the device operates, the carrier influx into the channel intensifies, leading to substantial shielding of electron-electron interactions. This is exemplified by degenerately doped ML $MoSe_2$. The GW-renormalized E_g of 1.59 eV aligns closely with the intrinsic E_g of 1.52 eV at the DFT-GGA level and the measured value of 1.58 eV obtained through angle-resolved photoemission spectroscopy [31,32]. Moreover, the validity of the DFT-NEGF method has been verified through the experimental realization of ultrathin FETs. In the actual transistors, material defects, impurities or device imperfections are usually unavoidable in fabrication processes [33–35]. However, the trilayer InSe transistors with a short channel of 10 nm exhibit an excellent crystal structure without visible defects [36]. This experimental research on the ultrashort transistor has approached the simulation limit. The simulation made by the DFT-NEGF method regarding transfer characteristics, I_{on}, delay time, power dissipation, and energy-delay products of the *n*-type carbon nanotube MOSFETs with $L_g = 5$ nm align closely with experimental counterparts [37,38]. Moreover, the prediction of the transfer characteristics, high I_{on}, low subthreshold swing, low delay time, low power dissipation and low energy-delay products of the InSe transistor is consistent with the latest experimental value (e.g., 1497 (simulation) vs 1430 (experiment) μA $μm^{-1}$ for I_{on}) [36,39]. The ballistic ratio has reached 83% in the 10-nm-L_g InSe FET in the experiment [36], and that is predicted to be nearly 90% in the MoS_2 FET at $L_g = 5$ nm [40]. Therefore, the ballistic transport is a good approximation in the sub-10 nm FET simulation.

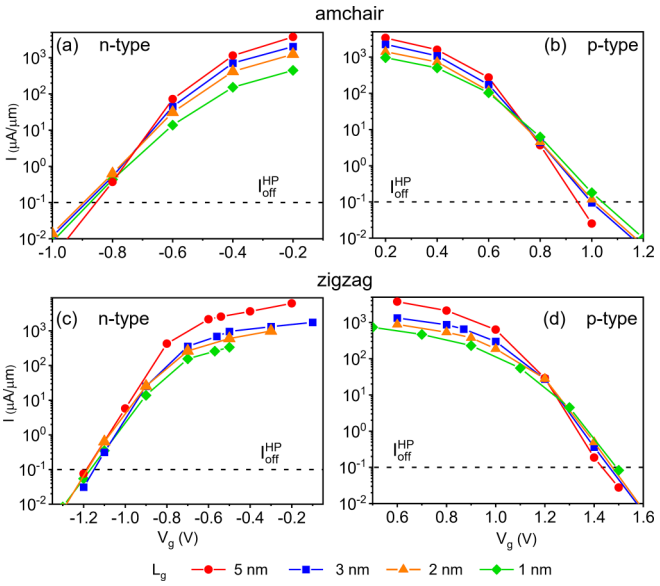

FIG. 2. I–V_g characteristics of the n− and p-type ML H-BAs MOSFETs along with the (a), (b) armchair and (c), (d) zigzag directions.

III. RESULTS AND DISCUSSION

A. Figures of merit

In terms of the ITRS and IRDS [18,19], most of the FOMs, such as current, capacitance, transconductance, and power-delay product (or power dissipation), are required to be normalized to width in the FETs both in the experiments and simulations [26,41–43]. For example, the off-state current and transconductance on the experiment have been width-normalized to 0.1 μA $μm^{-1}$ and 6 mS $μm^{-1}$, respectively [36]. The reason is that the width of the devices in various works might be different, and the width-normalized FOMs help to benchmark the devices. The width of the ML H-BAs transistor in our work is set to be periodic without energy quantization. The unit width is 5.9 Å in the zigzag-directed FET and 3.4 Å in the armchair-directed one (see Fig. S3 in the Supplemental Material for details) [20].

The on-state current I_{on} is vital for the performance of FETs, and a higher I_{on} indicates better device behavior. I_{on} can be calculated from the I_{ds}−V_g characteristics, where I_{ds} is the source-to-drain current and V_g is the gate voltage. I_{on} represents the current at on-state voltage $V_{g-on} = V_{dd} + V_{g-off}$. V_{dd} is the supply voltage, equal to the bias voltage V_b. In terms of the fitted data of the ITRS, V_{dd} is 0.55 ∼ 0.64 V when the gate length L_g is 1 ∼ 5 nm, and V_{g-off} is the off-state voltage at $I_{ds} = I_{off}$. The I_{on} standards are 406 ∼ 893 μA $μm^{-1}$ when L_g is 1 ∼ 5 nm, and the corresponding off-state current I_{off} is set to 0.1 μA $μm^{-1}$. Considering the optimized doping concentration, the $I_{ds} - V_g$ characteristics of the DG ML H-BAs MOSFETs with $L_g = 5$, 3, 2, and 1 nm are calculated, as shown in Figs. 2(a)–2(d) and Table II. The I_{on} values of both the n− and p-type armchair- and zigzag-directed ML

TABLE II. Benchmark of the device performances of the $n-$ and p-type double-gated (DG) monolayer (ML) BAs MOSFETs against the ITRS requirement for the HP application [6].

Direction	Doping type	L_g (nm)	L_{UL} (nm)	SS (mV dec^{-1})	I_{on} (μA μm^{-1})	g_m (mS μm^{-1})	C_t (fF μm^{-1})	τ (ps)	PDP (fJ μm^{-1})
		1	3	161	158	2.0	0.02	0.057	0.007
			4	117	228	1.5	0.01	0.020	0.003
	n-type	2	3	118	680	4.2	0.04	0.035	0.017
		3	2	103	1318	6.6	0.07	0.032	0.029
			3	91	1003	3.6	0.09	0.210	0.031
		5	1	88	3514	13	0.10	0.018	0.040
Armchair		1	3	198	42	0.3	0.02	0.054	0.007
			4	151	166	0.3	0.04	0.126	0.011
	p-type	2	3	126	562	3.1	0.03	0.029	0.009
		3	2	120	1081	4.5	0.04	0.021	0.015
			3	108	383	0.5	0.08	0.130	0.029
		5	1	92	2330	9.0	0.10	0.018	0.040
		1	5	122	260	0.9	0.02	0.034	0.005
	n-type	2	4	101	350	1.4	0.03	0.053	0.010
		3	3	100	695	3.0	0.07	0.055	0.023
Zigzag		5	1	106	2580	7.4	0.24	0.061	0.100
		1	5	115	175	0.9	0.02	0.051	0.005
	p-type	2	4	107	380	1.8	0.04	0.061	0.013
		3	3	106	658	2.9	0.07	0.058	0.023
		5	1	91	2200	7.4	0.24	0.063	0.097

H-BAs MOSFETs are shown in Fig. 3(a). The corresponding L_{UL} values are shown in Table III. Besides, those L_{UL} values are used in all the considered DG ML H-BAs MOSFETs hereafter. I_{on} generally decreases with the downscaling L_g for all of the considered FETs. When L_g of the armchair-directed FETs is scaled down from 5 to 1 nm, the corresponding values decrease from 3514 to 228 μA μm^{-1} for the n-type FETs and from 2330 to 166 μA μm^{-1} for the p-type FETs. In the zigzag-directed devices, the corresponding values decrease from 2580 to 260 μA μm^{-1} for the n-type FETs and from

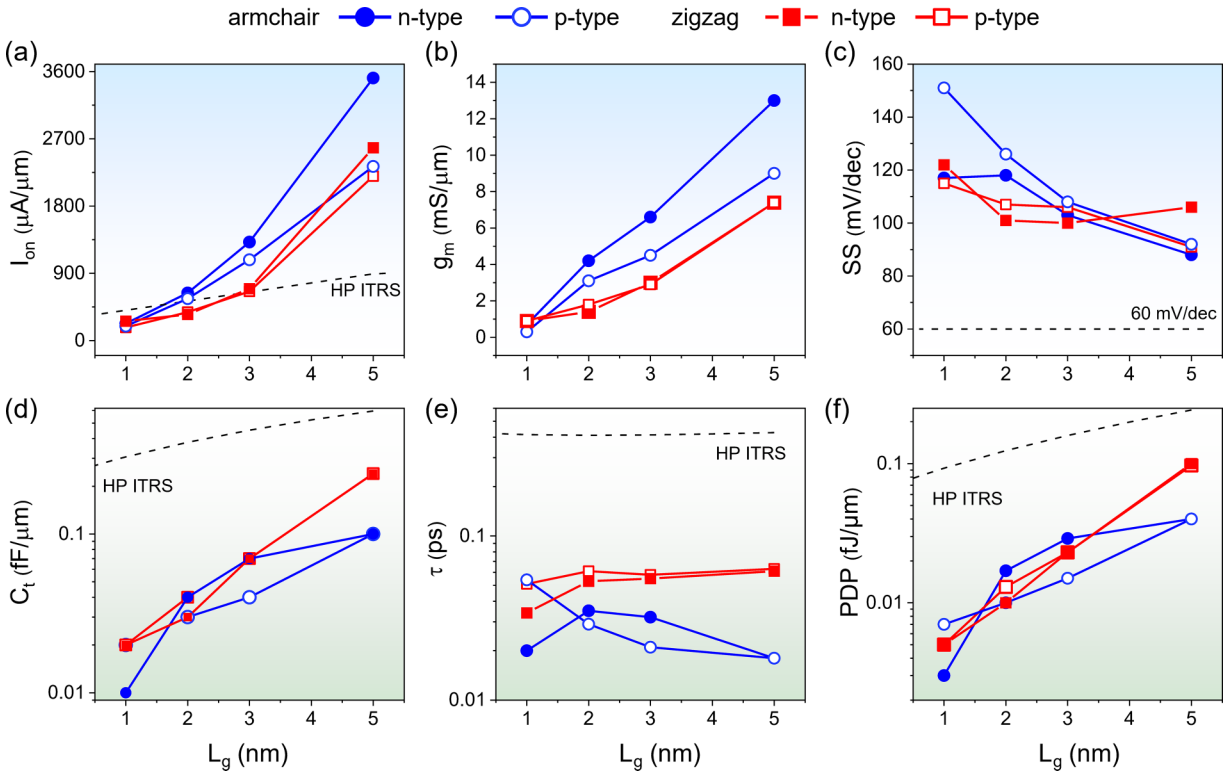

FIG. 3. Gate length L_g scaling of the (a) on-state current I_{on}, (c) transconductance g_m, (e) subthreshold swing SS, (d) total gate capacitance C_t, (e) delay time τ, (f) power dissipation PDP for the $n-$ and p-type ML H-BAs MOSFETs along with the armchair and zigzag directions.

TABLE III. The optimal underlap length for all the considered DG ML BAs MOSFETs hereafter.

	Underlap length (nm)	
Gate length (nm)	Armchair-oriented	Zigzag-oriented
5	1	1
3	2	3
2	3	4
1	4	5

2200 to 175 μA μm^{-1} for the *p*-type FETs. In addition, I_{on} of the armchair-directed *n*-type structure is generally higher than that of the zigzag-directed counterpart at a given L_g. For example, the former is over 30% higher than the latter when L_g is 5 nm. The reason lies in the much lower m_e^* of the armchair-directed ML H-BAs (0.17 vs 0.47 m_0). In terms of the ITRS, the scaling limit is 2 nm L_g for armchair-directed devices and 3 nm L_g for zigzag-directed ones for high-performance (HP) applications. Therefore, the ML H-BAs MOSFETs exhibit excellent immunity to short-channel effects (SCEs). Remarkably, the zigzag-directed devices show good symmetry for I_{on} of the *n*− and *p*-type devices. However, the symmetry of the *n*− and *p*-type armchair structures is worse due to the asymmetric effective mass (0.17 m_0 for m_e^* vs 0.44 m_0 for m_h^*).

Gate control is also important for transistors. Enhancing gate control is a key method to prevent SCE. The gate control in the superthreshold region is described by transconductance g_m using the equation $g_m = \frac{dI_{ds}}{dV_g}$. Besides, the gate control in the subthreshold region is described by subthreshold swing *SS* using the formula $SS = \frac{dV_g}{d(\log I_{ds})}$, where I_{ds} is the source-to-drain current, the same as the current *I* plotted in Fig. 2. The equation $d(\log I_{ds}) = \log I_1 - \log I_2 = \log(I_1/I_2)$ represents the order of magnitude change for the current, where I_1 and I_2 are the two current points in the subthreshold region. The higher g_m and lower *SS*, the higher the gate controllability. In Fig. 3(b), g_m of all of the considered ML H-BAs MOSFETs gradually decreases when L_g is scaled down from 5 to 1 nm. The symmetry for g_m is lost in the armchair-directed devices, and the corresponding g_m values range from 13 to 2 mS μm^{-1} (from 9 to 0.3 mS μm^{-1}) for the *n* (*p*)-type. However, the zigzag-directed devices show good symmetry for g_m of the *n*− and *p*-type ones, ranging from 7.4 to 2 mS μm^{-1} with $L_g = 5 \sim 1$ nm. The *SS* values of all of the considered ML H-BAs MOSFETs increase when L_g is scaled down from 5 to 1 nm. The results indicate weakened gate control with scaling L_g. The *SS* values of all of the considered ML H-BAs MOSFETs are comparable at a given L_g, ranging from 88 to 122 mV dec^{-1}.

Transistors with a large working speed and low power consumption are favorable for heat dissipation in CMOS ICs. The delay time τ ($\tau = \frac{C_t V_{dd}}{I_{on}}$) represents the time required for a transition from the on-state to the off-state in a device. V_{dd} is the supply voltage, equal to the bias voltage V_b. In terms of the fitted data of the ITRS, V_{dd} is $0.55 \sim 0.64$ V when the gate length L_g is $1 \sim 5$ nm. A lower τ indicates a higher operational speed. C_t is the total capacitance in the transistor and is three times the gate capacitance C_g ($C_g = \frac{\partial Q_{ch}}{W \partial V_g}$, Q_{ch} represents the charge from the channel), as specified by the ITRS. *W* is the unit width of the channel (3.4 and 5.9 Å along with the armchair and zigzag directions, respectively). In Fig. 3(d), the logarithmic coordinates visually enlarge the deviation when compared to the linear coordinate (see Fig. S4 in the Supplemental Material for details) [20]. Thus, we use logarithmic coordinates to show the data of C_t more clearly. C_t of all of the considered ML H-BAs MOSFETs gradually decreases when L_g is scaled down from 5 to 1 nm. The corresponding values range from 0.24 to 0.01 fF μm^{-1}, reaching the HP ITRS standards. However, there is no monotonic decrease in τ when L_g is scaled down because τ is not only proportional to C_t but also inversely proportional to I_{on} [Fig. 3(e)]. When L_g is 1 nm, τ of both the *n*− and *p*-type ML H-BAs MOSFETs along with the armchair and zigzag directions surpasses the HP ITRS standards ($0.410 \sim 0.426$ ps). In particular, the *n*− and *p*-type ML H-BAs MOSFETs along with the armchair direction show a lower τ at a given L_g than its zigzag-directed counterpart. This is because the armchair-directed ones have generally higher I_{on} and lower C_t. For instance, τ of the *n*-type armchair-directed one is 70% lower than that of its zigzag-directed counterpart due to its higher I_{on} (3514 vs 2580 μA μm^{-1}) and lower C_t (0.1 vs 0.24 fF μm^{-1}), The power dissipation (PDP) shows the energy cost associated with one on-off switching. PDP is proportional to C_t and V_{dd} ($PDP = C_t V_{dd}^2$) [41]. In Fig. 3(f), the scaling behavior of the PDP is the same as that of C_t. The PDP values of all the considered ML H-BAs MOSFETs can surpass the ITRS for HP applications ($0.007 \sim 0.100$ fJ μm^{-1} with $L_g = 1 \sim 5$ nm). They gradually decrease with the downscaling L_g because both the required V_{dd} and the C_t values are reduced.

The energy-delay products (EDPs) quantify the trade-off between energy consumption and the time it takes to perform a specific operation. The EDPs are expressed as EDP = $\tau \times$ PDP. The gray lines are the requirements of the ITRS (1.02×10^{-28} J s μm^{-1}) and IRDS (3.67×10^{-28} J s μm^{-1}) at the 2028 horizon for HP applications. A lower EDP value indicates more energy efficiency, which is also favorable for energy efficiency in CMOS ICs. The ML H-GaAs MOSFETs have been predicted to have the lowest EDPs among the simulated MOSFETs based on the typical ML channel materials in the 5-nm-L_g region [23]. Especially, the EDPs of both *n*-type and *p*-type ML H-BAs MOSFETs are comparable to those of their H-GaAs counterparts in the 5-nm-L_g region [Fig. 4(a)]. Besides, the EDPs of all the considered ML H-Bas MOSFETs gradually decrease when L_g is scaled down from 5 to 1 nm because of the decreased PDPs and the slightly changed τ, ranging from $1.7 \times 10^{-31} \sim 6.1 \times 10^{-30}$ J s μm^{-1}.

The on-state current I_{on} of the experimental *n*-type silicon (Si) Fin FETs with 5-nm gate length is 497 μA μm^{-1} [44]. Although both the source-drain voltage V_{ds} and dielectric permittivity ε_{ox} of the ML H-Bas FETs in this work are lower than those of such conventional Si-based FET (0.64 vs 1.0 V for V_{ds} and 3.9 vs 20 for ε_{ox}), the performance of the *n*-type ML H-Bas FET is still better than that of the conventional Si-based FET (e.g., ∼3000 vs 497 μA μm^{-1} for I_{on} and ∼100 vs 208 mV dec^{-1} for *SS*) [44]. Therefore, the ML H-BAs is a competitive alternative to Si to extend transistor miniaturization. Moreover, the current semiconductor technology

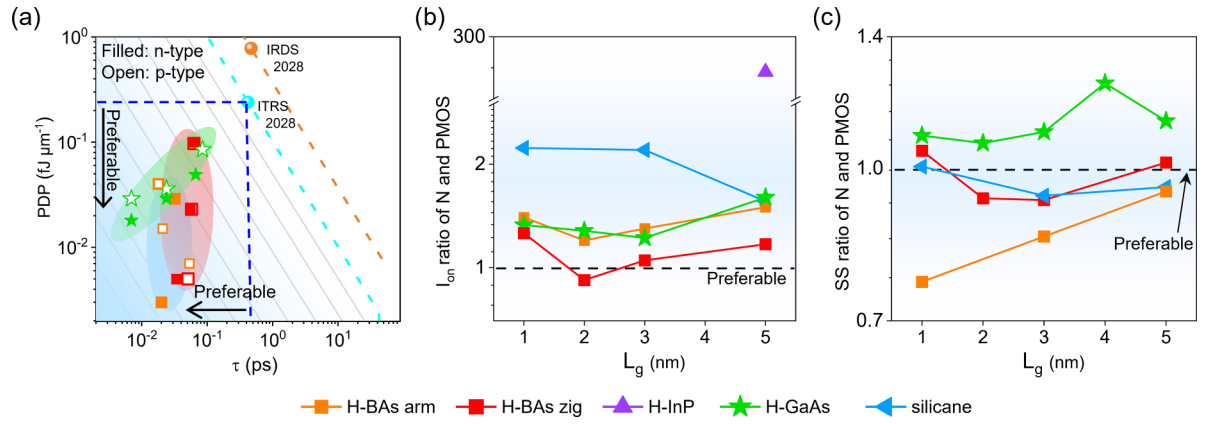

FIG. 4. (a) PDP versus τ of the $n-$ and p-type ML H-BAs MOSFETs along with the armchair and zigzag directions. The dashed lines represent PDP $= \frac{\text{EDP}}{\tau}$, where the EDP is the abbreviation of the energy-delay product. The ratio of (b) I_{on} and (c) SS between the NMOS and PMOS with the same channel material, including the ML H-BAs, H-GaAs, H-InP, and silicane [23,46,47].

advancing into the 1-nm scale is the technology node, corresponding to the physical 12-nm gate length [19]. Notably, the ML H-BAs FET can reach the IRDS and ITRS standards until the gate length is miniaturized to 2 nm. Therefore, the ML H-BAs FET with ultrashort gate length is prospective for next-generation electronics.

B. Symmetry of N and PMOS

The symmetry of n-type MOS (NMOS) and p-type MOS (PMOS) is very important for CMOS circuits. This is because NMOS and PMOS jointly complete logical operations and signal processing in CMOS circuits. If there is asymmetric performance between NMOS and PMOS, imbalanced amplification and transmission of the signal appear in the circuit, leading to logic errors or unreliable output [3,45]. Moreover, NP symmetry ensures lower power consumption. Therefore, symmetry of the FOMs for $n-$ and p-type FETs is desirable. However, III-V compound semiconductors usually suffer from asymmetric device performance. The reason lies in the asymmetric m_e^* and m_h^* in typical bulk III-V, leading to $10 \sim 100$ times higher electron mobility than hole mobility [3].

The ratio of I_{on} and SS between the $n-$ and p-type ML H-BAs MOSFETs is shown in Fig. 4(a, b). The ratio values of the ML H-GaAs, H-InP, and silicane FETs in the simulation are shown for comparison [23,46,47]. ML H-GaAs and ML H-InP are typical III-V materials, and silicane is the limiting form of Si. The ML H-InP and silicane FETs have the asymmetric performance of the $n-$ and p-type devices. For example, the I_{on} ratio of the $n-$ and p-type ML H-InP FETs is more than 200 [Fig. 4(a) [46]. The ML H-GaAs MOSFETs show more symmetry [23], and the I_{on} ratio is comparable to that of the armchair-directed ML H-BAs ($1.2 \sim 1.6$ at $L_g = 1 \sim 5$ nm). The symmetry of the $n-$ and p-type devices is well kept in the zigzag-directed ML H-BAs ones, and the corresponding I_{on} ratio is $0.92 \sim 1.26$ when L_g is $5 \sim 1$ nm, superior to those of other considered FETs. Meanwhile, the SS, τ, and PDPs values between the n-type and p-type zigzag-directed ones also exhibit good symmetry. For example, the SS ratio ranges from 0.94 to 1.06 at $L_g = 1 \sim 5$ nm [Fig. 4(c)], also showing better symmetry than other considered MOSFETs. The reason lies in that the m_e^* and m_h^* of the zigzag-directed ML H-BAs are symmetric (0.47 for m_e^* and 0.43 for m_h^*) while those in other considered channel materials are asymmetric (e. g., 0.10 for m_e^* and 0.53 for m_h^* in the ML H-GaAs) [23]. Therefore, the zigzag-directed ML H-BAs MOSFETs with symmetric FOMs exhibit great potential for future nanoelectronics.

C. Strain engineering

Strain engineering is an additional tool to boost the mobility of the channels, especially the compressive strain for the p-type III-V transistors [48,49]. Common strain resources, such as source/drain (S/D), strain-relaxed buffer, four-point wafer bending, and capping layer, have been used in the planar III-V transistors to enhance the p-type device performance [25,50–54].

The strain effect on the band structure of ML H-BAs is studied in this work, and the uniaxial strain $\alpha = -2 \sim -12\%$ is considered, as shown in Fig. 5. With increasing compressive strain, the conduction band minimum (CBM) gradually shifts down and the valence band maximum (VBM) shifts up. Therefore, the bandgap largely depends on the value of uniaxial strain. Three near-band-edge states A, B, and C can explain such bandgap-strain dependence. The Bloch state reflects the electron density distribution and wave function characteristics. The contour map of the Bloch state of states A-C is drawn, as shown in Fig. 6(a). According to equation $\Psi_k(r) = e^{ik\cdot r}u_k(r)$, the material structure determines the distribution of electrons at different energy levels. The general mechanism based on Heitler-London's exchange energy model could explain the variation in different energies with strain [55,56]. The different energy response trends with strain are closely related to the bonding/antibonding nature of the orbitals. The energies of the bonding and antibonding states in the Heitler-London model are given by the following equations:

$$E_{\text{bonding}} = 2E_0 + \frac{e^2}{R} + \frac{K + H_{ex}}{1 + S^2}, \tag{4}$$

$$E_{\text{antibonding}} = 2E_0 + \frac{e^2}{R} + \frac{K - H_{ex}}{1 - S^2}, \tag{5}$$

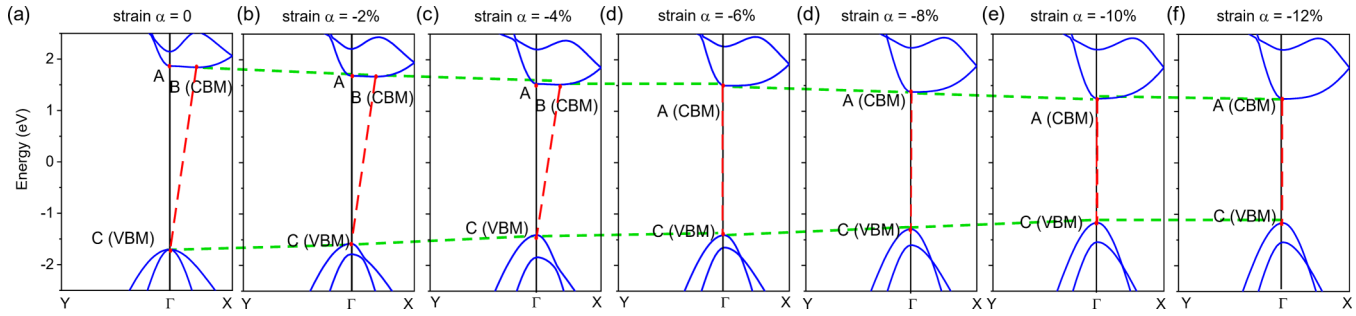

FIG. 5. (a)–(f) Energy band structure of ML H-BAs with and without the uniaxial compressive strain $\alpha = -2 \sim -12\%$ along with the armchair direction. The indirect/direct bandgap properties are the result of energy competition among the near-band-edge states A–C. Dashed lines indicate the energy shifts of CBM and VBM.

where E_0 is the energy of an isolated atom, the second term represents the energy of ion-ion interactions, K represents the classical Coulomb energy between electron-electron and electron-ion interactions, and S is the overlap integral of the orbitals between different atomic positions, which is usually much less than 1. S squared will be even smaller. Therefore, the exchange integral term (H_{ex}) will play a dominant role in determining the different energy variation behaviors with strain for the bonding and antibonding cases. The exchange integral term H_{ex} is given by

$$H_{ex} = \iint \psi_a^*(r_1)\psi_b^*(r_2)\left(\frac{1}{r_{12}} - \frac{1}{r_{2a}} - \frac{1}{r_{1b}}\right) \times \psi_b(r_1)\psi_a(r_2)dr_1dr_2, \quad (6)$$

where subscripts 1 and 2 represent the electrons of the two ions a and b, respectively, and the exchange integral term H_{ex} is contributed by the electron-electron interaction (i.e., $\frac{1}{r_{12}}$, positive) and the electron-ion interaction (i.e., $-\frac{1}{r_{2a}} - \frac{1}{r_{1b}}$, negative). For any hybrid orbitals where the electron density is not extremely localized, they have a large spatial distribution, usually spanning multiple atoms. The contribution of their electron-ion interactions dominates in exchange

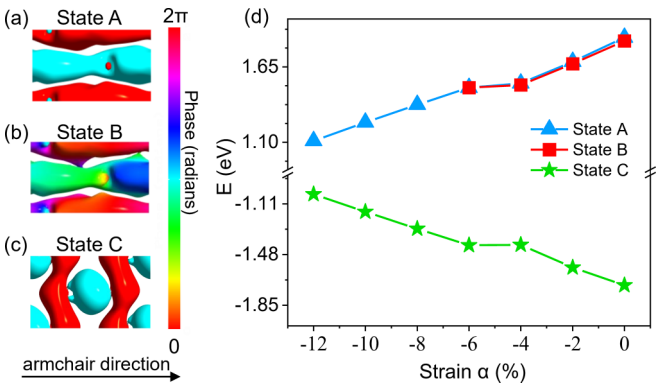

FIG. 6. (a)–(c) Bloch state energy contour diagram of near-band-edge states A–C of ML H-BAs under uniaxial strain $\alpha = -4\%$. States A and B are bonding along with the armchair direction while state C is antibonding. (d) The energy of near-band-edge states A-C as a function of applied uniaxial strain.

H_{ex}, corresponding to all states A, B, and C. As the atomic distance decreases (corresponding to the compressive strain), the energy contributed by the electron-ion interaction decreases more rapidly compared to the energy increase of the electron-electron contribution, leading to a decrease in the value of H_{ex}. The reduced H_{ex} value also results in a decrease in $E_{bonding}$ or an increase in $E_{antibonding}$.

Taking strain $= -4\%$ as an example [Figs. 6(a)–6(c)], states A and B bond along with the armchair direction, and the electron wave function has a coherent superposition between the atoms. The phase of the wave function between adjacent atoms is the same or continuous [Figs. 6(a) and 6(b)]. The exchange integral term H_{ex} values of states A and B all decrease with the compressive strain, and the corresponding energy will decrease in terms of Eq. (4). Notably, state A has a more uniform color in the armchair direction than that of state B, indicating a more concentrated phase distribution for the wave function and a higher degree of bonding. Therefore, the energy change of state A will be more sensitive than state B under the same compressive strain. When the uniaxial strain α is increased to -6%, state A at the Γ point replaces state B as the new CBM. State C is antibonding because its electronic wave function along with the armchair direction has an antiphase superposition between atoms, as shown in Fig. 6(c). The corresponding phase of the wave function between adjacent atoms is opposite or discontinuous, and the exchange integral term H_{ex} value decreases with the compressive strain, so the energy of state C will increase in terms of Eq. (5). Therefore, the VBM gradually moves up with the uniaxial compressive strain. Owing to the response of states A, B, and C, the bandgap of ML H-BAs is decreased under uniaxial compressive strain, and it transitions from indirect to direct at $\alpha = -6\%$.

To narrow the performance gap of the $n-$ and p-type armchair-directed devices, uniaxial compressive strains are applied to ML H-BAs along with the armchair direction. Only -2% and -4% strains are considered because they are the common compressive strain values in the actual FETs [49,51,57–60]. In Figs. 7(a) and 7(b), under the uniaxial strain along with the armchair direction, E_g linearly decreases from 3.68 to 3.37 and finally to 3.02 eV when α ranges from 0 to -2% and finally to -4%. Regulating the effective mass has been proven to be the primary mechanism influencing mobility in strained III-V group compound semiconductors and silicon

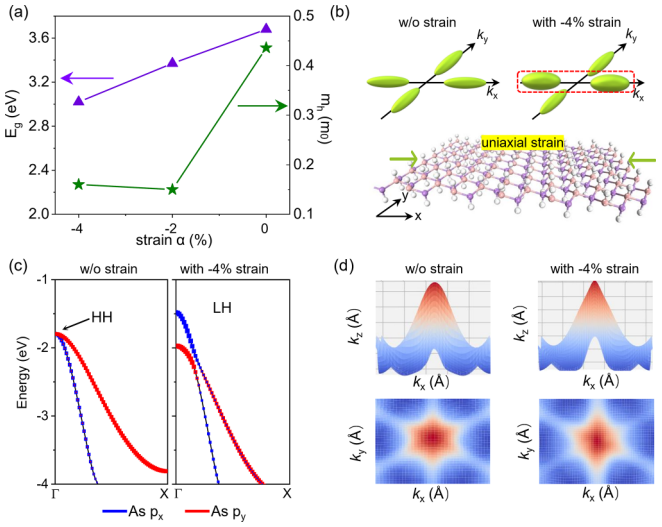

FIG. 7. (a) Band gap and hole effective mass under the uniaxial strain α for the ML H-BAs. (b) The $p_{x,y}$ orbitals of the ML-H-BAs valence band without and with strain (upper panel). The schematics of ML H-BAs under uniaxial compressive strain (lower panel). (c) The projected band structures of ML H-BAs onto the p_x and p_y orbitals. (d) The energy contour plots of the highest valence band of ML H-BAs without and with strain.

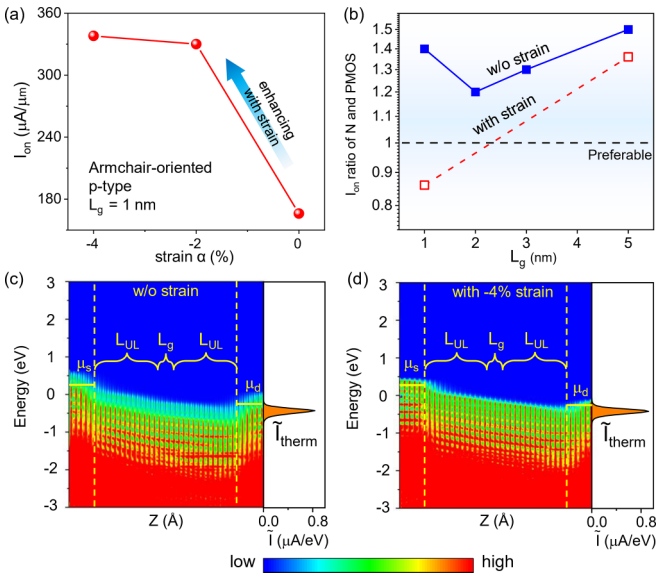

FIG. 8. (a) UL-optimized I_{on} for the p-type ML H-BAs MOSFET along with the armchair direction under the uniaxial strain α. (b) The N/PMOS ratio of I_{on} without and with uniaxial strain. (a) Local device density of states and spectral currents of the p-type ML H-BAs MOSFETs along with the armchair direction (c) without and (d) with uniaxial strain. Corresponding L_g and L_{UL} are 1 and 4 nm, respectively. $V_{dd} = (\mu_s - \mu_d)/e = 0.55$ V.

[50,61]. The m_h^* of ML H-BAs drastically decreases from 0.44 to 0.15 m_0 with α of -2% but is almost unchanged when α further decreases from -2% to -4%. When α is zero, the heavy- and light-hole bands degenerate at the Γ point [Fig. 7(c)], and the heavy-hole band is the topmost valence band, similar to typical III-V materials such as GaAs and InP [23,46]. As the uniaxial compressive strain increases, the light-hole band suddenly shifts up and becomes the topmost valence band at the Γ point. More p_x orbital charges of the As atoms accumulate in the topmost valence bands, especially at the Γ point [Figs. 7(b) and 7(c)]. The contour lines become steeper along with the armchair direction for the topmost band, leading to a reduced m_h^*.

The transport properties of the strained p-type ML H-BAs MOSFETs along with the armchair direction are calculated. Taking the 1-nm-L_g case as an example, the I_{on} values generally increase with increasing uniaxial compressive strains [Fig. 8(a)]. The I_{on} value drastically increases by over 80% (from 166 to 330 μA μm^{-1}) when α is from zero to 2% and slightly increases from 330 to 338 μA μm^{-1} when α is from 2% to 4%. Such a tendency is the same as that in m_h^* under strains. Therefore, the gap in I_{on} between the $n-$ and p-type ML H-BAs MOSFETs could be effectively decreased with the help of uniaxial compressive strain, and I_{on} of the p-type ML H-BAs MOSFET can even be higher than that of its n-type counterpart [Fig. 8(b)]. The local device density of states (LDDOS) and the spectral currents of the p-type ML H-BAs MOSFETs along with the armchair direction without and with uniaxial strain are shown in Figs. 8(c) and 8(d). The LDDOS near the valence band edge in the channel region significantly accumulates with uniaxial compressive strain. The corresponding peak spectral current is also higher than that without strain (0.92 vs 0.83 μA eV^{-1}), leading to a higher I_{on} (166 vs 338 μA μm^{-1}). Therefore, the device can be effectively controlled by the strain, and the symmetry of the $n-$ and p-type armchair-directed devices can be improved with appropriate strain values. The influence of the strain effects on the zigzag-oriented ML H-BAs FETs has also been considered. Similar to the device performance of the armchair-oriented one, I_{on} of the p-type zigzag-oriented ML H-BAs FETs is also improved with the increasing uniaxial compressive strain (see Fig. S5 in the Supplemental Material for details) [20]. The I_{on} value is increased from 175 to 205 and finally to 330 μA μm^{-1} when uniaxial strain α is changed from 0 to -1% and finally to -2%. The main reason is the broken valence band degeneracy at the Γ point, similar to the armchair-oriented one.

IV. CONCLUSION

In summary, we use *ab initio* quantum transport methods to predict the transport properties of monolayer ML H-BAs FETs. Both the armchair- and zigzag-oriented ML H-BAs FETs can meet the requirements of the ITRS even if L_g is scaled down to 2 and 3 nm, respectively. Moreover, the zigzag-oriented ML H-BAs FETs preserve the same good symmetry of $n-$ and p-type as bulk FETs. In contrast, the symmetry of the armchair-oriented ones is not satisfactory. Nevertheless, applying uniaxial compressive strain to p-type armchair-oriented FETs effectively mitigates such asymmetry. The reason is that the valence band degeneracy is broken, and the light-hole band becomes the topmost valence band. Therefore, both $n-$ and p-type ML H-BAs MOSFETs along with the armchair and zigzag directions are prospective for next-generation electronics.

ACKNOWLEDGMENTS

This work was supported by the Ministry of Science and Technology of China (No. 2022YFA1203904), the National Natural Science Foundation of China (No. 12274002), the Fundamental Research Funds for the Central Universities, the Natural Science Basic Research Program of Shaanxi (Program No. 2022JM-051), the High-performance Computing Platform of Peking University, and the MatCloud + high throughput materials simulation engine.

The authors declare no conflicts of interest.

[1] S. Das, A. Sebastian, E. Pop, C. J. McClellan, A. D. Franklin, T. Grasser, T. Knobloch, Y. Illarionov, A. V. Penumatcha, J. Appenzeller, Z. Chen, W. Zhu, I. Asselberghs, L.-J. Li, U. E. Avci, N. Bhat, T. D. Anthopoulos, and R. Singh, Nat. Electron. **4**, 786 (2021).

[2] C. Liu, H. Chen, S. Wang, Q. Liu, Y.-G. Jiang, D. W. Zhang, M. Liu, and P. Zhou, Nat. Nanotechnol. **15**, 545 (2020).

[3] J. Shin, G. A. Gamage, Z. W. Ding, K. Chen, F. Tian, X. Qian, J. W. Zhou, H. Lee, J. S. Zhou, L. Shi, T. Nguyen, F. Han, M. D. Li, D. Broido, A. Schmidt, Z. F. Ren, and G. Chen, Science **377**, 437 (2022).

[4] Y. Liu, X. Duan, H.-J. Shin, S. Park, Y. Huang, and X. Duan, Nature (London) **591**, 43 (2021).

[5] S. B. Samavedam, J. Ryckaert, E. Beyne, K. Ronse, N. Horiguchi, Z. Tokei, I. Radu, M. G. Bardon, M. H. Na, A. Spessot, and S. Biesemans, Future logic scaling: towards atomic channels and deconstructed chips, *2020 IEEE International Electron Devices Meeting (IEDM) 12–18 Dec. 2020* (IEEE, New York, 2020), pp 1.1.1-1.1.10.

[6] J. S. Kang, M. Li, H. Wu, H. Nguyen, T. Aoki, and Y. Hu, Nat. Electron. **4**, 416 (2021).

[7] Y. Cui, Z. Qin, H. Wu, M. Li, and Y. Hu, Nat. Commun. **12**, 1284 (2021).

[8] S. Yue, F. Tian, X. Y. Sui, M. Mohebinia, X. X. Wu, T. Tong, Z. M. Wang, B. Wu, Q. Zhang, Z. F. Ren, J. M. Bao, and X. F. Liu, Science **377**, 433 (2022).

[9] S. Li, M. Tian, Q. Gao, M. Wang, T. Li, Q. Hu, X. Li, and Y. Wu, Nat. Mater. **18**, 1091 (2019).

[10] X. Lü, S. He, H. Lian, S. Lv, Y. Shen, W. Dong, and Q. Duan, Appl. Surf. Sci. **531**, 147262 (2020).

[11] S. Ullah, P. A. Denis, and F. Sato, ACS Omega **3**, 16416 (2018).

[12] Q. Hang, F. Wang, P. D. Carpenter, D. Zemlyanov, D. Zakharov, E. A. Stach, W. E. Buhro, and D. B. Janes, Nano Lett. **8**, 49 (2008).

[13] P. Laukkanen, M. P. J. Punkkinen, M. Kuzmin, K. Kokko, J. Lång, and R. M. Wallace, Appl. Phys. Rev. **8**, 011309 (2021).

[14] H.-Y. Cheung, S. Yip, N. Han, G. Dong, M. Fang, Z.-x. Yang, F. Wang, H. Lin, C.-Y. Wong, and J. C. Ho, ACS Nano **9**, 7545 (2015).

[15] J. P. Perdew, K. Burke, and M. Ernzerhof, Phys. Rev. Lett. **77**, 3865 (1996).

[16] M. Brandbyge, J. L. Mozos, P. Ordejon, J. Taylor, and K. Stokbro, Phys. Rev. B **65**, 165401 (2002).

[17] S. Smidstrup, T. Markussen, P. Vancraeyveld, J. Wellendorff, J. Schneider, T. Gunst, B. Verstichel, D. Stradi, P. A. Khomyakov, U. G. Vej-Hansen, M.-E. Lee, S. T. Chill, F. Rasmussen, G. Penazzi, F. Corsetti, A. Ojanperä, K. Jensen, M. L. N. Palsgaard, U. Martinez, A. Blom, M. Brandbyge, and K. Stokbro, J. Phys.: Condens. Matter **32**, 015901 (2019).

[18] The International Technology Roadmap for Semiconductors (ITRS) 2013 Edition. https://www.semiconductors.org/resources/2013-international-technology-roadmap-for-semiconductors-itrs/.

[19] The International Roadmap for Devices and Systems (IRDS). https://irds.ieee.org/editions/2022.

[20] See Supplemental Material at http://link.aps.org/supplemental/10.1103/PhysRevMaterials.8.014603 for the fitted values for the sub-5 nm gate length region, in terms of the Requirements of the International Technology Roadmap for Semiconductors for the high-performance application, and concentration test of the monolayer H-BAs MOSFETs. Schematic view of the ML H-BAs MOSFETs along with the armchair and zigzag directions. Gate length scaling of the total gate capacitance with logarithmic and linear coordinates. The strain effect on the zigzag ML H-BAs MOSFETs.

[21] A. R. Williams, P. J. Feibelman, and N. D. Lang, Phys. Rev. B **26**, 5433 (1982).

[22] S. Datta, *Electronic Transport in Mesoscopic Systems* (Cambridge University Press, Cambridge, 1995).

[23] Q. Li, S. Fang, S. Liu, L. Xu, L. Xu, C. Yang, J. Yang, B. Shi, J. Ma, J. Yang, R. Quhe, and J. Lu, ACS Appl. Mater. Interfaces **14**, 23597 (2022).

[24] S. Liu, Q. Li, C. Yang, J. Yang, L. Xu, L. Xu, J. Ma, Y. Li, S. Fang, B. Wu, J. Dong, J. Yang, and J. Lu, Phys. Rev. Appl. **18**, 054089 (2022).

[25] Q. Li, C. Yang, L. Xu, S. Liu, S. Fang, L. Xu, J. Yang, J. Ma, Y. Li, B. Wu, R. Quhe, K. Tang, and J. Lu, Adv. Funct. Mater. **33**, 2214653 (2023).

[26] S. B. Desai, S. R. Madhvapathy, A. B. Sachid, J. P. Llinas, Q. Wang, G. H. Ahn, G. Pitner, M. J. Kim, J. Bokor, C. Hu, H.-S. P. Wong, and A. Javey, Science **354**, 99 (2016).

[27] J. Ryou, Y.-S. Kim, S. Kc, and K. Cho, Sci. Rep. **6**, 29184 (2016).

[28] Y. Wang, S. Liu, Q. Li, R. Quhe, C. Yang, Y. Guo, X. Zhang, Y. Pan, J. Li, H. Zhang, L. Xu, B. Shi, H. Tang, Y. Li, J. Yang, Z. Zhang, L. Xiao, F. Pan, and J. Lu, Rep. Prog. Phys. **84**, 056501 (2021).

[29] T. Eknapakul, P. D. C. King, M. Asakawa, P. Buaphet, R. H. He, S. K. Mo, H. Takagi, K. M. Shen, F. Baumberger, T. Sasagawa, S. Jungthawan, and W. Meevasana, Nano Lett. **14**, 1312 (2014).

[30] M. Luo, Y. H. Shen, and J. H. Chu, Jpn. J. Appl. Phys. **55**, 093001 (2016).

[31] Y. Liang and L. Yang, Phys. Rev. Lett. **114**, 063001 (2015).

[32] S. Liu, J. Li, B. Shi, X. Zhang, Y. Pan, M. Ye, R. Quhe, Y. Wang, H. Zhang, J. Yan, L. Xu, Y. Guo, F. Pan, and J. Lu, J. Mater. Chem. C **6**, 7400 (2018).

[33] A. C. Ford, J. C. Ho, Y.-L. Chueh, Y.-C. Tseng, Z. Fan, J. Guo, J. Bokor, and A. Javey, Nano Lett. **9**, 360 (2009).

[34] K. S. Yi, K. Trivedi, H. C. Floresca, H. Yuk, W. Hu, and M. J. Kim, Nano Lett. **11**, 5465 (2011).

[35] F. Wang, S. Yip, N. Han, K. Fok, H. Lin, J. J. Hou, G. Dong, T. Hung, K. S. Chan, and J. C. Ho, Nanotechnology **24**, 375202 (2013).
[36] J. Jiang, L. Xu, C. Qiu, and L.-M. Peng, Nature (London) **616**, 470 (2023).
[37] X. Sun, L. Xu, Y. Zhang, W. Wang, S. Liu, C. Yang, Z. Zhang, and J. Lu, ACS Appl. Mater. Interfaces **12**, 20633 (2020).
[38] R. Wu, Q. Tao, J. Li, W. Li, Y. Chen, Z. Lu, Z. Shu, B. Zhao, H. Ma, Z. Zhang, X. Yang, B. Li, H. Duan, L. Liao, Y. Liu, X. Duan, and X. Duan, Nat. Electron. **5**, 497 (2022).
[39] Y. Wang, R. Fei, R. Quhe, J. Li, H. Zhang, X. Zhang, B. Shi, L. Xiao, Z. Song, J. Yang, J. Shi, F. Pan, and J. Lu, ACS Appl. Mater. Interfaces **10**, 23344 (2018).
[40] L. Liu, Y. Lu, and J. Guo, IEEE Trans. Electron Devices **60**, 4133 (2013).
[41] R. Quhe, L. Xu, S. Liu, C. Yang, Y. Wang, H. Li, J. Yang, Q. Li, B. Shi, Y. Li, Y. Pan, X. Sun, J. Li, M. Weng, H. Zhang, Y. Guo, L. Xu, H. Tang, J. Dong, J. Yang, Z. Zhang, M. Lei, F. Pan, and J. Lu, Phys. Rep. **938**, 1 (2021).
[42] L. Xie, M. Liao, S. Wang, H. Yu, L. Du, J. Tang, J. Zhao, J. Zhang, P. Chen, X. Lu, G. Wang, G. Xie, R. Yang, D. Shi, and G. Zhang, Adv. Mater. **29**, 1702522 (2017).
[43] K. Xu, D. Chen, F. Yang, Z. Wang, L. Yin, F. Wang, R. Cheng, K. Liu, J. Xiong, Q. Liu, and J. He, Nano Lett. **17**, 1065 (2017).
[44] H. Lee, L. E. Yu, S. W. Ryu, J. W. Han, K. Jeon, D. Y. Jang, K. H. Kim, J. Lee, J. H. Kim, S. Jeon, G. Lee, J. Oh, Y. Park, W. Bae, H. Lee, J. Yang, J. Yoo, S. Kim, and Y. K. Choi, Sub-5nm all-around gate FinFET for ultimate scaling, *2006 Symposium on VLSI Technology, 2006. Digest of Technical Papers* (IEEE, New York, 2006), pp 13–15.
[45] Z. Zhang, S. Wang, Z. Wang, L. Ding, T. Pei, Z. Hu, X. Liang, Q. Chen, Y. Li, and L.-M. Peng, ACS Nano **3**, 3781 (2009).
[46] L. Xu, R. Quhe, Q. Li, S. Liu, J. Yang, C. Yang, B. Shi, H. Tang, Y. Li, X. Sun, J. Yang, and J. Lu, J. Mater. Chem. C **10**, 2223 (2022).
[47] Y. Pan, J. Dai, L. Xu, J. Yang, X. Zhang, J. Yan, J. Li, B. Shi, S. Liu, H. Hu, M. Wu, and J. Lu, Phys. Rev. Appl. **14**, 024016 (2020).
[48] C. Jia, Z. Lin, Y. Huang, and X. Duan, Chem. Rev. **119**, 9074 (2019).
[49] G. Signorello, S. Sant, N. Bologna, M. Schraff, U. Drechsler, H. Schmid, S. Wirths, M. D. Rossell, A. Schenk, and H. Riel, Nano Lett. **17**, 2816 (2017).
[50] L. Balaghi, S. Shan, I. Fotev, F. Moebus, R. Rana, T. Venanzi, R. Hübner, T. Mikolajick, H. Schneider, M. Helm, A. Pashkin, and E. Dimakis, Nat. Commun. **12**, 6642 (2021).
[51] Z. Zhu, J. Svensson, A. R. Persson, R. Wallenberg, A. V. Gromov, and L.-E. Wernersson, Nano Res. **13**, 2517 (2020).
[52] E. Barrigón, M. Heurlin, Z. Bi, B. Monemar, and L. Samuelson, Chem. Rev. **119**, 9170 (2019).
[53] J. A. del Alamo, Nature (London) **479**, 317 (2011).
[54] M. Chu, Y. Sun, U. Aghoram, and S. E. Thompson, Annu. Rev. Mater. Res. **39**, 203 (2009).
[55] X. Peng, Q. Wei, and A. Copple, Phys. Rev. B **90**, 085402 (2014).
[56] R. M. White, *Quantum Theory of Magnetism* (Springer, Berlin, 1983), Vol. 32.
[57] S. W. Bedell, A. Khakifirooz, and D. K. Sadana, MRS Bull. **39**, 131 (2014).
[58] D. Shahrjerdi and S. W. Bedell, Nano Lett. **13**, 315 (2013).
[59] Y. Kang, S. Xu, K. Han, E. Y. J. Kong, Z. Song, S. Luo, A. Kumar, C. Wang, W. Fan, G. Liang, and X. Gong, Nano Lett. **21**, 5555 (2021).
[60] L. Witters, H. Arimura, F. Sebaai, A. Hikavyy, A. P. Milenin, R. Loo, A. D. Keersgieter, G. Eneman, T. Schram, K. Wostyn, K. Devriendt, A. Schulze, R. Lieten, S. Bilodeau, E. Cooper, P. Storck, E. Chiu, C. Vrancken, P. Favia, E. Vancoille, J. Mitard, R. Langer, A. Opdebeeck, F. Holsteyns, N. Waldron, K. Barla, V. D. Heyn, D. Mocuta, and N. Collaert, IEEE Trans. Electron Dev. **64**, 4587 (2017).
[61] D. Yu, Y. Zhang, and F. Liu, Phys. Rev. B **78**, 245204 (2008).